

BiO_mF_n/BiO_xI_y/GO Nanocomposites: Synthesis, characterization, and photocatalytic activity

Jing-Ya Fu, Li-Wen Chen, Yong-Ming Dai, Fu-Yu Liu, Shih-Tsuen Huang, Chiing-Chang Chen*

Department of Science Education and Application, National Taichung University of Education, Taichung, 403, Taiwan



ARTICLE INFO

Keywords:

Bismuth oxyfluoride
Bismuth oxyiodide
Graphene oxide
Composites
Photocatalytic

ABSTRACT

This is the first paper to report a series of bismuth oxyfluoride/bismuth oxyiodide/graphene oxide (BiO_mF_n/BiO_xI_y/GO) nanocomposites with different GO contents that were synthesized through a simple hydrothermal method and characterized using X-ray diffraction, transmission electron microscopy, scanning electron microscopy–energy dispersive spectroscopy, Fourier transform infrared spectroscopy, X-ray photoelectron spectroscopy, Brunauer–Emmett–Teller specific surface areas, and UV–vis diffuse reflectance spectroscopy. The BiO_mF_n/BiO_xI_y/GO composites exhibited excellent photocatalytic activities in the degradation of crystal violet (CV) and 2-hydroxybenzoic acid (HBA) under visible-light irradiation. The order of rate constants appears to be Bi₅₀O₅₉F₃₂/BiOI/GO > BiOF/BiOI/GO > BiOI > Bi₅₀O₅₉F₃₂/BiOI/Bi₅O₇I/GO > BiOF > GO. The photocatalytic activity of Bi₅₀O₅₉F₃₂/BiOI/GO composites reached a maximum rate constant of 0.2539 h⁻¹, which is 1.1 times higher than that of Bi₅₀O₅₉F₃₂/BiOI and 1.3 and 110 times higher than those of BiOI and Bi₅₀O₅₉F₃₂, respectively.

1. Introduction

Researchers have considerably been concerned with semiconductor photocatalysis galvanized by visible light, and this is because this process affords a valuable means of solving problems associated with environmental pollution and energy supply. A photocatalyst that is inexpensive and also environmentally potent is integral to practical photocatalysis applications [1]. The aforementioned process has been substantially focused on for eliminating toxic materials from wastewater. Researchers have used several systems to subject crystal violet (CV) dyes to photocatalytic degradation in order to produce active species, which include BiO_xCl_y/BiO_mI_n (identified through ultraviolet–visible (UV–Vis) diffuse reflectance spectra) [2], BiOBr/BiOI [3], BaTiO₃ [4], BiOI [5], Bi₂WO₆ [6], PbBiO₂Br/BiOBr [7], BiOI/GO [8], Bi₂SiO₅/g-C₃N₄ [9], and SrFeO_{3-x}/g-C₃N₄ [10]. A strategy that can simply and effectively improve a photocatalyst's photocatalytic activity entails heterostructure incorporation; this strategy exhibits substantial potential for tuning photocatalyst electronic properties to the desired levels and realizing photoinduced electron–hole pair separation efficiently.

Scholars have extensively investigated bismuth oxyhalide compounds (BiOX, X = F, Cl, Br, and I) because of their chemical stability, unique layer structure, and excellent photocatalytic performance when subjected to UV–Vis illumination. The increasing interest garnered by

BiOX can be attributed to its favorable properties, namely appropriate energy gaps, high stability, and superior photocatalytic activity levels when compared with other compounds [11,12]. Among the aforementioned compounds, BiOF possesses a direct band gap (approximately 3.5 eV), thus rendering this photocatalyst sensitive to UV radiation. The BiOF atomic structure comprises [Bi₂O₂]²⁺ slabs between the pair of fluorine atoms [F₂]²⁻, thus giving rise to layers of [Bi₂O₂F₂]. Nevertheless, I_{5p} and O_{2p} orbitals mostly constitute the valence band of bismuth oxyiodides, whereas the Bi_{6p} orbital constitutes the conduction band [13]; therefore, as demonstrated previously, the band-gap energy of iodine-poor BiO_mI_n is lower than that of Bi₂O₃ but higher than that of BiOI [14]. Consequently, the mentioned materials are conceivably suitable for application as photocatalysts exhibiting responsiveness to visible light. Specifically, the BiO_mI_n structure and composition have a strong effect on its physicochemical properties such as oxidizing abilities and optical and electronic properties; this consequently offers a window to derive new photocatalysts that can be used to degrade environmental and toxic pollutants effectively. The first report on BiOX/BiOY systems (X, Y = Cl, Br, and I) possessing approximately unlimited solubility can be traced back to Keller and Kramer [15]; since this report, scholars have published several articles reporting the successful synthesis of similar oxyhalide materials as well as their unique photocatalytic properties. Nevertheless, until recently, reports of the synthesis approaches, characterization, and assessed features of an array of

* Corresponding author.

E-mail address: ccchen@mail.ntcu.edu.tw (C.-C. Chen).

BiOX/BiOY have remained rare.

Graphene (GR) and GR derivatives possess unique two-dimensional (2D) structures and superior conductivity to other materials, thus rendering them outstanding electron mediators; these materials have also garnered substantial attention recently [16]. Therefore, GR is an ideal support material because of its favorable adsorption activity and interfacial contact. The structure of GR is powerful yet flexible, and GR has high carrier mobility. Consequently, hybrid photocatalysts based on GR, including BiOI/GR [17] and BiOBr/GR, exhibit excellent photocatalytic efficiency [18]. Research on GR can be divided into two specific branches, with one branch investigating graphene oxide (GO) and the other investigating reduced GO (rGO). This could thus be regarded a precursor of semiconductor/GO (or rGO) growth, in which thermal processes or chemical processes are applied. As revealed by previous research, incorporating GO into a metal oxide can engender enhanced photocatalytic activity [19–21].

According to a literature review conducted by the authors, no study has reported on the photocatalytic degradation of CV dyes under the assistance of $\text{BiO}_m\text{F}_n/\text{BiO}_x\text{I}_y/\text{GO}$ and under visible-light irradiation. Accordingly, this study applied a simple hydrothermal method to synthesize a series of $\text{BiO}_m\text{F}_n/\text{BiO}_x\text{I}_y/\text{GO}$ nanocomposites with different GO contents; the photocatalytic activities of these compounds in terms of CV degradation in aqueous media when irradiated with visible light were compared. This paper also proposes and describes the possible mechanisms underlying the photodegradation process. The study contributes to the literature on synthesizing $\text{BiO}_m\text{F}_n/\text{BiO}_x\text{I}_y/\text{GO}$ and degrading dyes for future applications in environmental pollution regulation.

2. Experiment

2.1. Materials

The entirety of the applied chemicals in this study was of analytic grade, with no subsection to additional purification. The following, in addition, were purchased: HBA (2-hydroxybenzoic acid or salicylic acid), $\text{Bi}(\text{NO}_3)_3 \cdot 5\text{H}_2\text{O}$, KI, KF (Katayama), KCl (Shimakyu), CV dye (TCI), sodium azide (Sigma), *p*-benzoquinone (Alfa Aesar), isopropanol (Merck), and ammonium oxalate (Osaka). Furthermore, reagent-grade ammonium acetate, sodium hydroxide, nitric acid, and HPLC-grade methanol were obtained from Merck.

2.2. Instruments and analytical methods

Scanning electron microscopy-energy dispersive spectroscopy (SEM-EDS) was measured using a JEOL JSM-7401 F microscope, with the acceleration voltage being set to 15 kV. Moreover, a JEOL-2010 microscope was applied for the measurement of transmission electron microscopy (TEM) images, EDS spectra, high-resolution TEM images, and selected-area electron diffraction patterns, with the acceleration voltage being set at 200 kV. High-resolution X-ray photoelectron spectroscopy (XPS) was recorded with an ULVAC-PHI spectrometer. Al-K α radiation was also realized at 15 kV; a Scinco SA-13.1 spectrophotometer recorded ultraviolet–visible (UV–Vis) DRS data within the 300–800 nm wavelength range at room temperature. A diffractometer system (MAC Science MXP18) applying Cu-K α radiation (40 kV and 80 mA) recorded X-ray diffraction (XRD) patterns. UV photoelectron spectroscopy data were measured with an ULVAC-PHI XPS PHI Quantera SXM, and photoluminescence (PL) data were measured with a Hitachi F-7000. An automated system (Micromeritics Gemini) recorded the samples' Brunauer–Emmett–Teller (BET) specific surface areas (S_{BET}) at 237 °C; in this process, nitrogen gas was utilized as the adsorbate at liquid-nitrogen temperature. Finally, a Brüker ER200D spectrometer, with an Agilent 5310A frequency counter operating in the X band, recorded EPR spectra at 77 K.

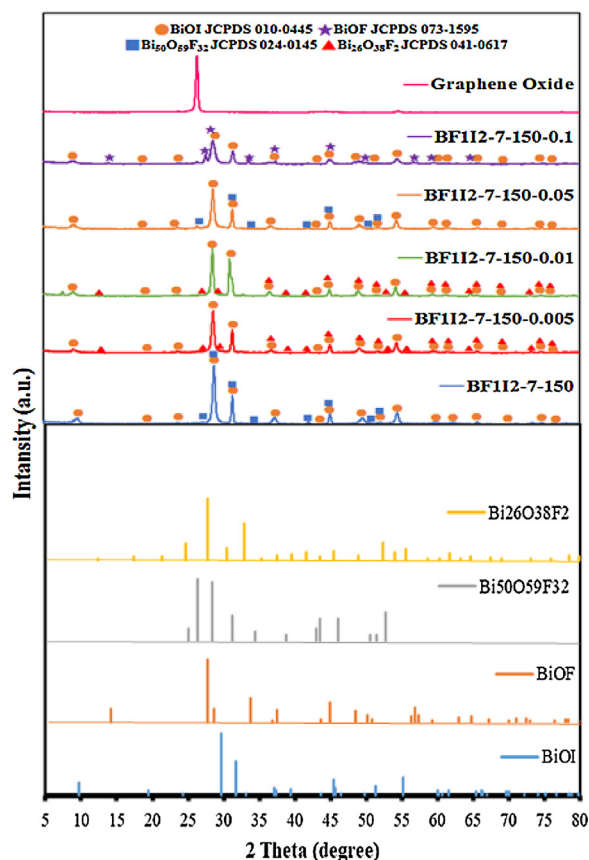


Fig. 1. XRD patterns of as-prepared $\text{BiO}_m\text{F}_n/\text{BiO}_x\text{I}_y/\text{GO}$ samples with different amounts of GO. (Hydrothermal conditions: molar ratio KF:KI = 1:2, GO = 0–0.1 g, pH = 7, temperature = 150 °C, time = 12 h).

2.3. Synthesis of $\text{BiO}_m\text{F}_n/\text{BiO}_x\text{I}_y/\text{GO}$

Graphene oxide (GO) was prepared by stirring 1 g of powdered flake graphite and 0.5 g of sodium nitrate into 23 mL of sulfuric acid in a 0 °C ice bath. While maintaining vigorous agitation, 3 g potassium permanganate was added to the dispersion. The ice bath was then removed, and the temperature of the dispersion was raised to 35 °C and maintained at that temperature overnight. Subsequently, potassium permanganate (3 g) was added to the dispersion, which was allowed to stand for 3 h. Subsequently, 46 mL of water was slowly stirred into the paste, causing violent effervescence and raising the temperature to 95 °C. The diluted suspension, now brown in color, was maintained at this temperature for 15 min. The suspension was then further diluted with approximately 140 mL of warm water and treated with 30% (w) hydrogen peroxide to reduce the residual permanganate and manganese dioxide to bleach the soluble manganese sulfate. Upon treatment with peroxide, the dispersions became bright yellow. The dispersions were filtered, and a yellow-brown filter cake was obtained. After washing the cake five times with a total of 140 mL warm water, the GO residue was dispersed in 100 mL of 10% hydrochloric acid. Dry GO was obtained through centrifugation followed by drying in an oven at 60 °C overnight [8,22].

First, 5 mmol bismuth nitrate was mixed in a 50-mL flask and then added to 5 mL of 4 M ethylene glycerol and GO powder. Stirring continuously, 2 M of sodium hydroxide was added dropwise to adjust the pH value; when a precipitate was formed, 2 mL of potassium iodide and potassium fluoride were also added dropwise. The solution was then stirred vigorously for 30 min and transferred into a 30 mL Teflon-lined autoclave, which was heated to 100–250 °C for 12 h and then naturally cooled to room temperature. The resulting solid precipitate was

Table 1

Crystalline phase changes of as-prepared samples under different hydrothermal conditions. (Hydrothermal conditions: molar ratio KF/KI = 1/2, GO = 0–0.1 g, temp = 150 °C, pH = 1–13, time = 12 h). ● BiOI ◆ Bi₅O₇I ☆ BiOF ■ Bi₅₀O₅₉F₃₂ ▲ Bi₂₆O₃₈F₂.

Temperature = 150 °C	GO (g)				
	0	0.005	0.01	0.05	0.1
pH value	0	0.005	0.01	0.05	0.1
1	● ☆	● ☆	● ☆	● ☆	● ☆
4	● ☆	● ☆	● ☆	● ☆	● ☆
7	● ■	● ▲	● ▲	● ▲	● ☆
10	● ◆ ▲	● ◆ ▲	● ◆ ▲	● ◆ ▲	● ◆ ▲
13	◆ ▲	● ◆ ▲	● ◆ ▲	● ◆ ▲	● ◆ ▲

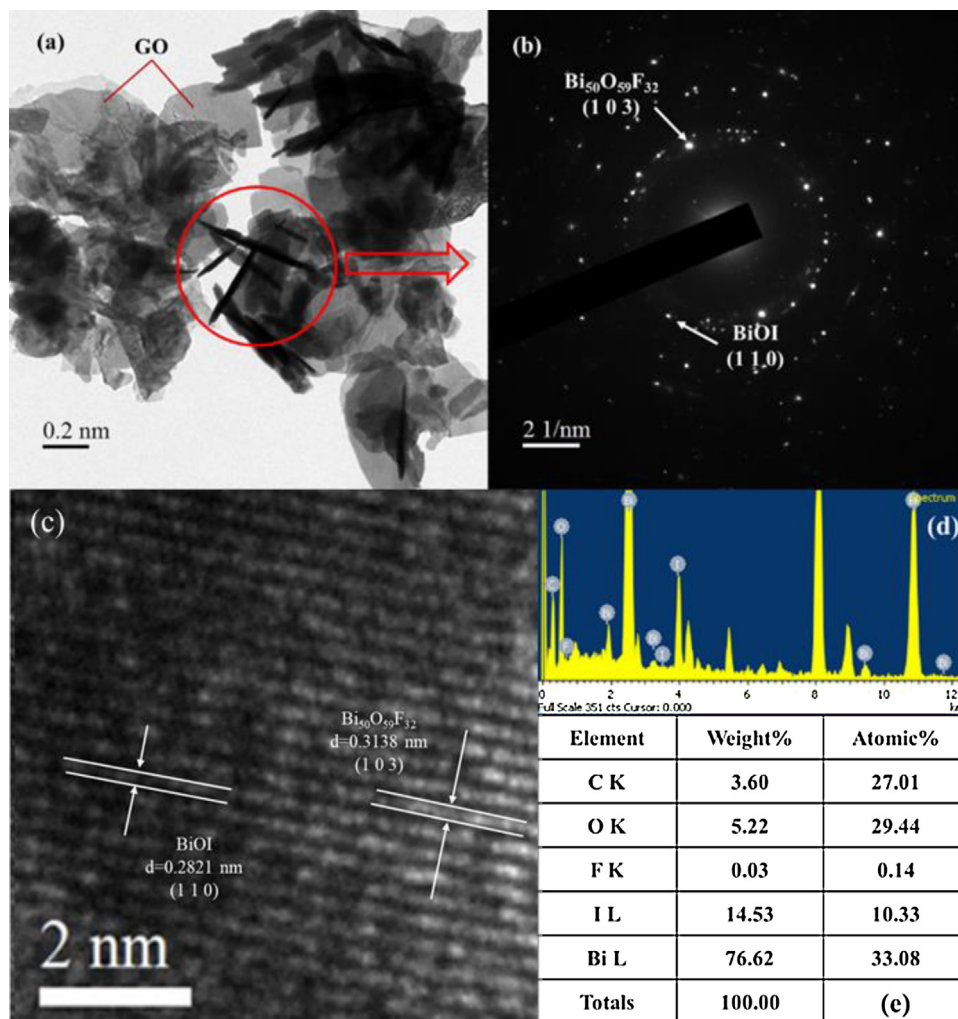


Fig. 2. (a) FE-SEM image, (b) SAD, (c) HR-TEM image, and (d) and (e) EDS of the Bi₅₀O₅₉F₃₂/BiOI/GO (BF112-7-150-0.05) sample using the hydrothermal autoclave method.

collected through filtration, washed with deionized water and methanol to remove any possible ionic species in the solid precipitate, and then dried at 60 °C overnight. Depending on the molar ratio of bismuth nitrate to potassium iodide or potassium fluoride, pH value, temperature, and time, different BiO_mF_n/BiO_xI_y/GO samples could be synthesized.

2.4. Photocatalytic and active species experiments

In the trials of this study, we chose either HBA (or CV) as our target pollutant to evaluate photocatalytic activity. HBA (or CV) irradiation products were immersed in stirred aqueous solutions housed in flasks

(100 mL); both an aqueous dispersion of 10 ppm 100 mL HBA (or CV) and 10 mg of the photocatalyst were then placed in a Pyrex flask. The suspension's pH was adjusted through sodium hydroxide or nitric acid solution addition. Dark experiments were performed in order to examine the adsorption/desorption equilibrium. Prior to the irradiation, the suspension was magnetically stirred in dark for ca. 30 min to establish an adsorption/desorption equilibrium between the CV (or HBA) and the catalyst surface. After batch sorption experiments had been conducted, the mixture underwent a centrifugation procedure conducted at 3000 rpm to determine the absorbance of HBA (or CV) at 298 (or 588) nm through UV-PDA. Irradiation was supplied by 10-W Xe arc

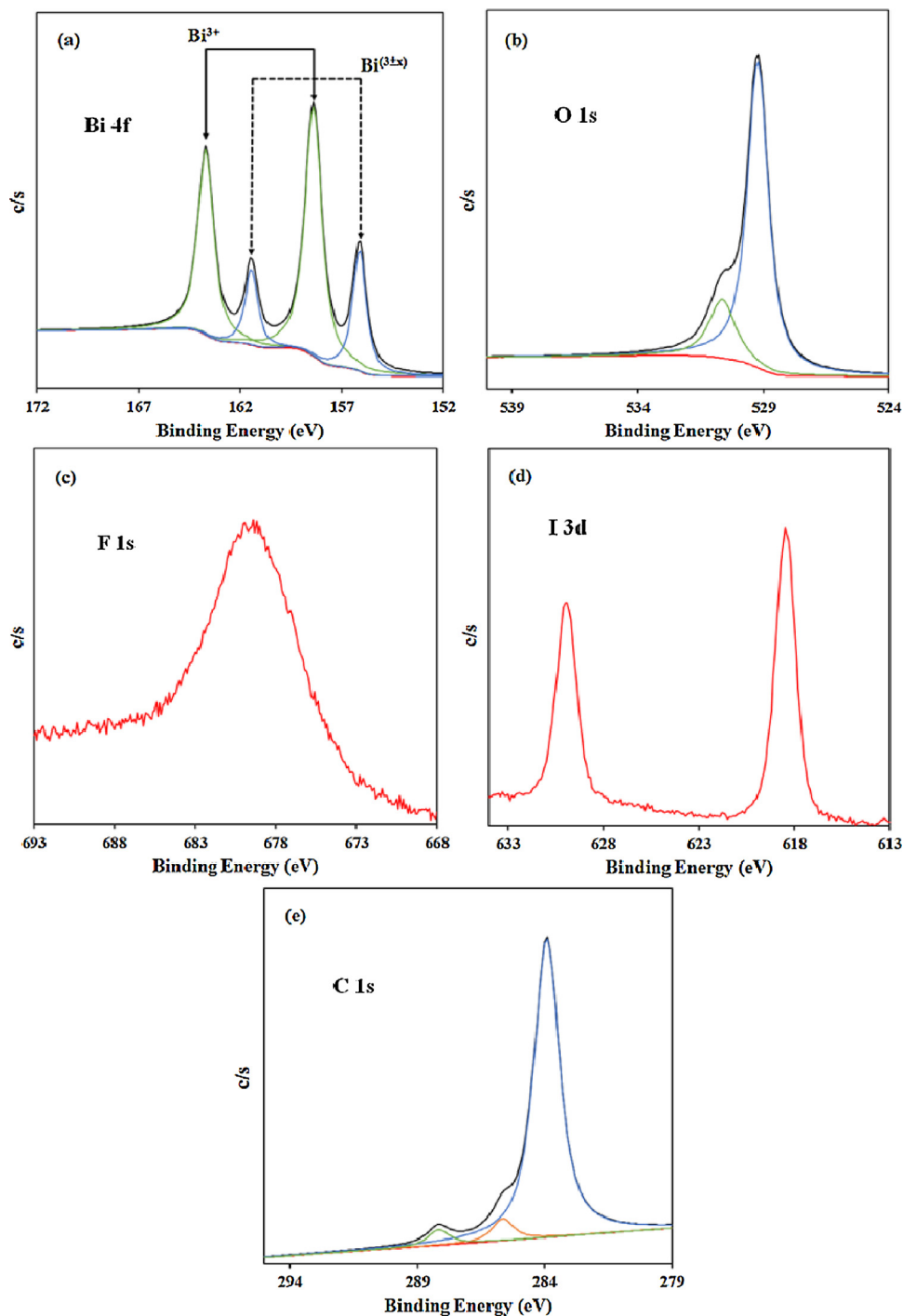


Fig. 3. XPS spectra of the as-prepared $\text{Bi}_{50}\text{O}_{59}\text{F}_{32}/\text{BiOI}/\text{GO}$ (BF112-7-150-0.05) sample. (a) Bi 4f; (b) O 1s; (c) F 1s; (d) I 3d; and (e) C 1s.

lamps at a fixed light intensity of 3.2 W/m^2 , with a distance of 30 cm separating the reaction vessel and the light source. At specified irradiation time intermissions, 5-mL aliquots were collected and then underwent a centrifugation procedure for photocatalyst removal, and each supernatant sample was subsequently analyzed through UV-PDA.

A series of quenchers were introduced to scavenge the relevant active species to evaluate the effect of the active species during the photocatalytic reaction. Superoxide radicals, hydroxyl radicals, holes, and singlet oxygen ($^1\text{O}_2$) were studied by adding 1.0 mM benzoquinone (BQ; a quencher of superoxide radicals), 1.0 mM isopropanol (IPA; a quencher of hydroxyl radicals), 1.0 mM ammonium oxalate (AO; a quencher of holes), and 1.0 mM sodium azide (SA, a quencher of singlet

oxygen). The method was similar to that of a previously reported photocatalytic activity test [2,3].

3. Results and discussion

3.1. Characterization of $\text{BiO}_m\text{F}_n/\text{BiO}_x\text{I}_y/\text{GO}$ composites

Figs. 1 and S1 of supplementary data illustrate the XRD patterns derived for the as-prepared samples, indicating the existence of different $\text{BiO}_m\text{F}_n/\text{BiO}_x\text{I}_y/\text{GO}$ phase composites. The results revealed the BiOF phase in all as-prepared samples (JCPDS 73-1595), $\text{Bi}_{50}\text{O}_{59}\text{F}_{32}$ phase (JCPDS 24-0145), $\text{Bi}_{26}\text{O}_{38}\text{F}_2$ phase (JCPDS 41-0617), BiOI phase

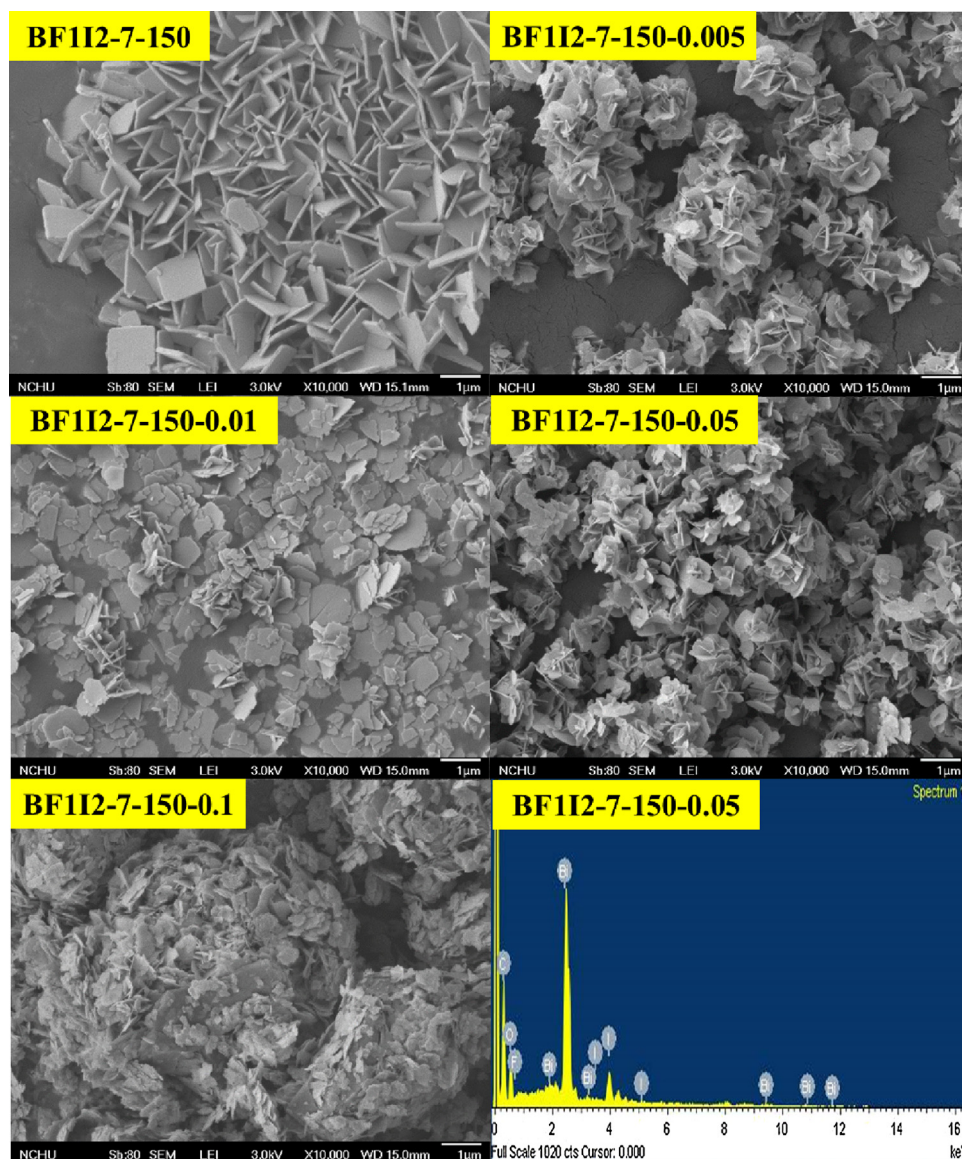


Fig. 4. SEM images of the samples prepared through the hydrothermal method with different amounts of GO. (Hydrothermal conditions: molar ratio KF:KI = 1:2, temperature = 150 °C, pH = 7, time = 12 h).

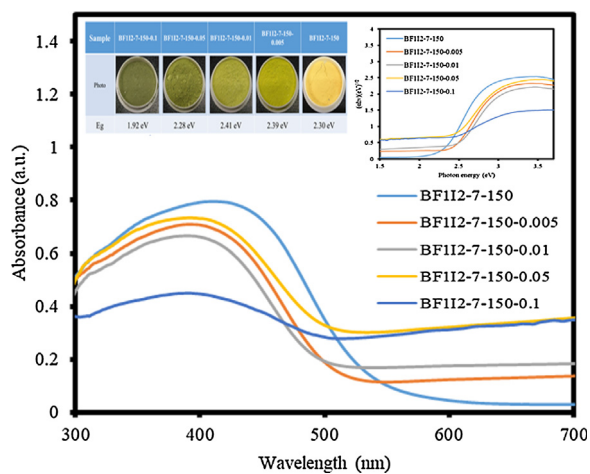


Fig. 5. UV-vis absorption spectra of the as-prepared photocatalysts under different amounts of GO (hydrothermal conditions: molar ratio KF:KI = 1:2, GO = 0–0.1 g, temperature = 150 °C, pH = 7, time = 12 h).

(JCPDS 10-0445), $\text{Bi}_7\text{O}_9\text{I}_3$ phase [23], $\text{Bi}_5\text{O}_7\text{I}$ phase (JCPDS 40-0548), and GO [24]. For GO = 0 g, the XRD patterns are the same as those recorded for $\text{Bi}_{50}\text{O}_{59}\text{F}_{32}/\text{BiOI}/\text{GO}$ ternary phases; for GO = 0.05–0.05 g, the XRD patterns are identical to those reported for $\text{Bi}_{26}\text{O}_{38}\text{F}_{22}/\text{BiOI}/\text{GO}$ ternary phases; and for GO = 0.1 g, the XRD patterns and the patterns derived for $\text{BiOF}/\text{BiOI}/\text{GO}$ ternary phases were determined to be identical. The XRD measurement results derived at different pH values and GO amounts are summarized in Table 1.

As evidenced by high-resolution transmission electron microscopy (Fig. 2), two lattice image sets were found, wherein the associated d-spacing was 0.3138 and 0.2827 nm, which corresponded to the (103) plane of $\text{Bi}_{50}\text{O}_{59}\text{F}_{32}$ and the (110) plane of BiOI [8], an adequately concordant outcome with the XRD results (Fig. 1). A series of $\text{BiO}_m\text{F}_n/\text{BiO}_x\text{I}_y$ phases were synthesized in the composites, as suggested by the results, and the synthesized phases facilitated separating the corresponding photoinduced carriers, thereby engendering high photocatalytic activity levels.

A series of changes were demonstrated, by the results, to occur in the products at the various aforementioned pH values. The determined changes, expressed as $\text{BiOF} \rightarrow \text{Bi}_{50}\text{O}_{59}\text{F}_{32} \rightarrow \text{Bi}_{26}\text{O}_{38}\text{F}_{22} \rightarrow \alpha\text{-Bi}_2\text{O}_3$ and

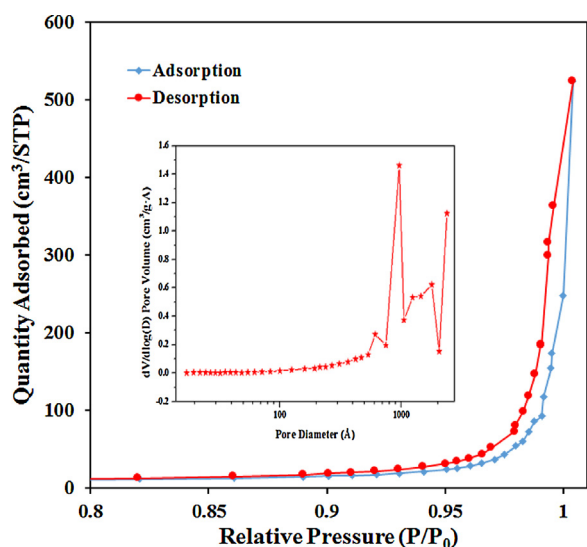


Fig. 6. N_2 adsorption–desorption isotherm distribution curves and the pore distribution curves of $Bi_{50}O_{59}F_{32}/BiOI/GO$ (BF112-7-150-0.05) (inset). (hydrothermal conditions: Molar ratio KF:KI = 1:2, temperature = $150^\circ C$, pH = 7, time = 12 h).

$BiOI \rightarrow Bi_4O_5I_2 \rightarrow Bi_7O_9I_3 \rightarrow Bi_3O_4I \rightarrow Bi_5O_7I \rightarrow \alpha-Bi_2O_3$, occurred under different hydrothermal conditions. Different bismuth oxyhalide compositions were obtained by controlling the pH level of the hydrothermal reaction.

The prepared samples' purity was measured through X-ray photoelectron spectroscopy (XPS). Bi 4f, O 1s, F 1s, and I 3d spectra were derived for the $Bi_{50}O_{59}F_{32}/BiOI/GO$ samples (Fig. 3). As demonstrated by the transition peaks involved in the orbitals of these spectra, Bi, O, F, I, and C constituted the catalysts. The distinctive binding energy derived for Bi 4f_{7/2} was 157.5–158.4 eV (Fig. 3(a)), demonstrating oxidation state derived for bismuth to be trivalent. Moreover, in all samples, an extra spin-orbit doublet exhibiting a measured binding energy of 155.2–156.0 eV was determined for Bi 4f_{7/2}; this implies some bismuth sections exist in the valence state of (+3–x). Accordingly, the hydrothermal method engendered the fractional reduction of the trivalent bismuth to the lower valence state. Liao et al. [2,5] have revealed a similar chemical shift for Bi 4f_{7/2}, namely approximately 2.0 eV. The mentioned authors determined that the Bi substoichiometric forms could explain the formal oxidation state observed for Bi (+3–x) in the interior of the Bi_2O_3 layer; additionally, in the determined crystal lattice, the established low oxidation state engendered oxygen vacancies. Nevertheless, this study assumed the formal oxidation state observed for Bi (+3–x) to have been engendered by the Bi substoichiometric forms existing at the particles' outer site. In addition, the established low oxidation state could engender oxygen vacancies on the observed crystal surface; thus, for the samples' bismuth element, the primary chemical states are demonstrated to be nontrivalent. High-resolution XPS spectra, as illustrated in Fig. 3(b), were derived for the $Bi_{50}O_{59}F_{32}/BiOI/GO$ composites' O 1s region. The derived spectra were resolved into two peaks: a main peak (528.6 eV), ascribed to the bonds between Bi and O observed in the BiO_x layered structure's (Bi_2O_3)²⁺ slabs, and a secondary peak (530.9 eV), ascribed to the hydroxyl groups dwelling on the surface [25]. The binding energy that was derived for F 1s was 686.2 eV, according to Fig. 3(c); this are ascribable to F that existed at the monovalent oxidation state. The binding energies that were derived for I 3d_{5/2} and 3d_{3/2} were 628.9 and 617.4 eV, respectively, according to Fig. 3(d); these could be ascribed to I that existed at the monovalent oxidation state. Fig. 3(e) is an illustration of C 1s spectra at high resolution derived for $Bi_{50}O_{59}F_{32}/BiOI/GO$ composites and pure GO, primarily revealing the carbon species unoxidized carbons (sp^2 carbon), C–O, and C=O. Fig. 3(e) reveals three different

chemically shifted components; subjecting these components to a deconvolution process yielded sp^2 carbons existing in aromatic rings (284.3 eV) and C atoms that were determined as being bonded to oxygen (C–O 286.7 eV) and carbonyl (C=O, 288.6 eV) [26]. Fig. 3(b) presents an asymmetric peak for O 1s; the XPS peak-fitting package designed for pure GO was applied to split this peak, with the 529.9-eV peak being considered to be related to the surface-adsorbed water molecule or the external –OH group and the 528.6-eV O 1s peak being considered to be related to the bonds between C and O existing in GO [2].

In this study, the hydrothermal method was applied at various pH values to yield a series of $BiO_mF_n/BiO_xI_y/GO$ composites, whose surface morphologies were examined through the use of FE-SEM-EDS. Figs. 4 and S2 present the derived FE-SEM images for these samples, revealing square-plate, flower-like, nanosheet, small-thin nanosheet, and irregular small-thin nanosheet morphologies. The derived samples primarily comprised bismuth, oxygen, fluorine, iodine, and carbon, as demonstrated by SEM-EDS and TEM-EDS. Thus, the controlled hydrothermal method could be applied for synthesizing, through a selective process, a series of $BiO_mF_n/BiO_xI_y/GO$ composites.

As revealed by the UV–Vis absorption spectra that were derived for various $BiO_mF_n/BiO_xI_y/GO$ composites (Figs. 5 and S3), the absorption edge of BiO_mF_n/BiO_xI_y was approximately 540 nm. The E_g value of $BiO_mF_n/BiO_xI_y/GO$ was determined as 1.92–2.30 eV, after plotting $(ah\nu)^{1/2}$ against energy ($h\nu$). The results suggest that the fabricated $BiO_mF_n/BiO_xI_y/GO$ composites exhibited considerable improvements in terms of optical absorption properties and solar light efficiency, a property beneficial for enhancing photocatalytic activity.

The BET surface area of GO was measured as $12.98\text{ m}^2\text{g}^{-1}$, which is considerably lower than the theoretical evaluation derived for fully exfoliated pristine graphene (approximately $2620\text{ m}^2\text{g}^{-1}$). Moreover, for GO, the calculated pore volume and size were $0.016\text{ cm}^3\text{g}^{-1}$ and 5.32 nm, respectively. This study obtained isotherms for GO, and they were determined to approximate Type III isotherms not accompanied by a hysteresis loop observed at a relatively high pressure of 0.6–1.0 [2], which suggests nonporous GO. The BiO_xI_y and BiO_mF_n isotherms were determined to approximate Type IV isotherms along with a hysteresis loop observed at a relatively high of 0.6–1.0 [2]. Fig. 6 presents isotherm curves derived by plotting nitrogen adsorption against nitrogen desorption for $Bi_{50}O_{59}F_{32}/BiOI/GO$. The BET surface area of the sample was $18.2\text{ m}^2\text{g}^{-1}$. Pore volume and size values of $0.269\text{ cm}^3/\text{g}$ and 8761 nm, respectively, were determined for $Bi_{50}O_{59}F_{32}/BiOI/GO$. The isotherms were determined to approximate Type IV isotherms along with a hysteresis loop—exhibiting a similar shape to H3—observed at a relatively high pressure of 0.6–1.0. Here, the similarity in shape to H3 indicates that pores similar to slit and typically created by aggregating plate-like particles existed, a finding matching the findings obtained from the FE-SEM process and the nanoplate-like morphology of the samples that was self-assembled. Thus, the self-assembled nanosheets form hierarchical architectures.

3.2. Photocatalytic activity

Fig. 7 displays the variations of the UV–Vis spectra that were assessed during CV and HBA photodegradation executed in aqueous $Bi_{50}O_{59}F_{32}/BiOI/GO$ dispersions under irradiation with visible light. Around 99% of the CV and HBA were completely degraded after 24 h of this irradiation. The characteristic CV dye absorption band is at approximately 589.1 nm. When the dye was processed through irradiation using visible light, the band rapidly decreased along with small hypochromic shifts (553.8 nm); however, the results did not reveal an additional absorption band nor did they indicate a band in the UV range ($\lambda > 200\text{ nm}$); this thus suggests the formation of a sequence of N-demethylated intermediates and indicates that the entirety of the CV dye's conjugated chromophore structure may have undergone a cleavage process. With the application of further irradiation, the absorption band

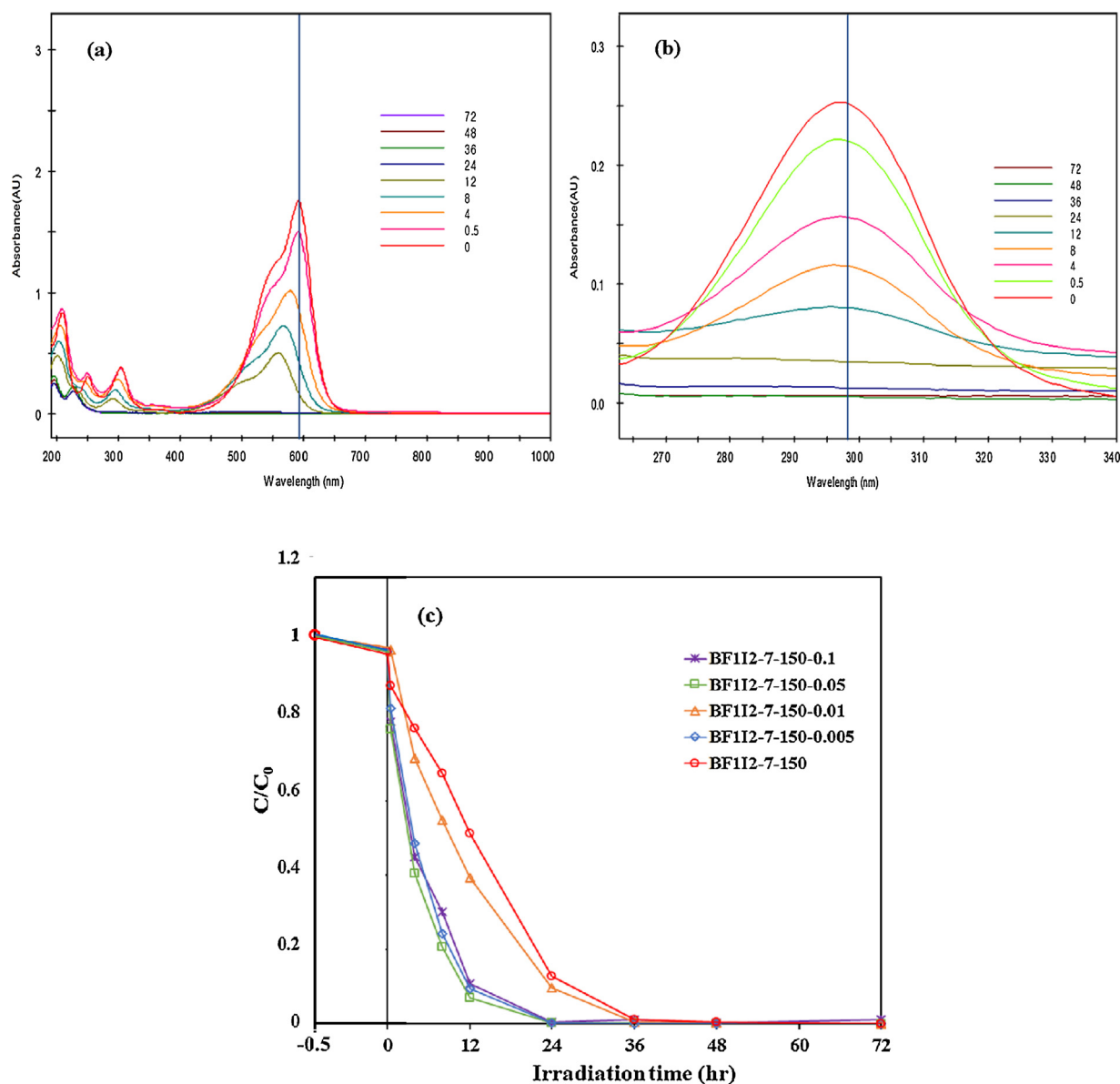


Fig. 7. (a) (b) Temporal UV-vis adsorption spectra of CV and HBA and (c) photocatalytic degradation of CV as a function of irradiation time with various photocatalysts. (Hydrothermal condition: molar ratio KF:KI = 1:2, GO = 0–0.1 g, pH = 7, reaction temperature = 150 °C, reaction time 12 h; 10 mg/100 mL photocatalyst, 10 ppm CV).

at 553.8 nm was reduced, but the results did not reveal any further shift in wavelength; on the basis of these results, this absorption band (i.e., 553.8 nm) could be considered to be the band of the full *N*-de-methylated product of the applied CV dye [2,6].

The degradation efficiency is derived as a function of reaction time in Figs. 7(c) and S4; using 0.005–0.1 g of $\text{BiO}_m\text{F}_n/\text{BiO}_x\text{I}_y/\text{GO}$ composites resulted in a significant removal efficiency enhancement. Dark experiments were performed in order to examine the adsorption/desorption equilibrium. Prior to the irradiation, the suspension was magnetically stirred in dark for ca. 30 min to establish an adsorption/desorption equilibrium between the CV (or HBA) and the catalyst surface. It was also observed that the C/C_0 from 1.0 to 0.96—the former was in the initial dye concentration while the latter was added 0.005–0.1 g of $\text{BiO}_m\text{F}_n/\text{BiO}_x\text{I}_y/\text{GO}$ to 100 mL solution. For the derivation of a clearer comprehension of the reaction kinetics that were associated with CV degradation, this study applied an apparent pseudo-first-order model [27] in the experiments, namely $\ln(C_0/C) = kt$. The data that are presented in Table 2 were subjected to a first-order linear fit; consequently, the $\text{Bi}_{50}\text{O}_{59}\text{F}_{32}/\text{BiOI}/\text{GO}$ composite's k value was derived as

$2.539 \times 10^{-1} \text{ h}^{-1}$ (the maximum degradation rate), a value considerably exceeding those derived for the other composites. The rate constants derived for the diverse photocatalysts were compared (Table 2) and can be ordered as follows: $\text{Bi}_{50}\text{O}_{59}\text{F}_{32}/\text{BiOI}/\text{GO} > \text{BiOF}/\text{BiOI}/\text{GO} > \text{BiOI} > \text{Bi}_{50}\text{O}_{59}\text{F}_{32}/\text{BiOI}/\text{Bi}_5\text{O}_7\text{I}/\text{GO} > \text{BiOF} > \text{GO}$. The maximum rate constant related to the $\text{Bi}_{50}\text{O}_{59}\text{F}_{32}/\text{BiOI}/\text{GO}$ composite's photocatalytic activity was 0.2539 h^{-1} , a value that exceeded those of $\text{Bi}_{50}\text{O}_{59}\text{F}_{32}/\text{BiOI}$, BiOI, and $\text{Bi}_{50}\text{O}_{59}\text{F}_{32}$ by 1.1, 1.3, and 110 times, respectively.

To evaluate the durability of the $\text{Bi}_{50}\text{O}_{59}\text{F}_{32}/\text{BiOI}/\text{GO}$ composite, this study recycled the previously used catalyst. Through the utilization of centrifugation, the catalyst was collected after each cycle. After the removal of CV in the third cycle, the study did not observe any apparent deficit in photocatalytic activity, and the observed deficit was 10% during the fifth run (Fig. 8(a)). After examining the previously used $\text{Bi}_{50}\text{O}_{59}\text{F}_{32}/\text{BiOI}/\text{GO}$ using XRD, the study determined no difference between this sample and the as-prepared sample (Fig. 8(b)); hence, the $\text{Bi}_{50}\text{O}_{59}\text{F}_{32}/\text{BiOI}/\text{GO}$ composite has excellent photostability.

The enhanced photocatalytic activities of $\text{BiO}_m\text{F}_n/\text{BiO}_x\text{I}_y/\text{GO}$ are

Table 2

Pseudo-first-order rate constants for the degradation of CV with photocatalysts under visible-light irradiation. (Hydrothermal conditions: molar ratio KF: KI = 1:2, GO = 0–0.1 g, temp = 150 °C, pH = 1–13, time = 12 h.).

Sample	k (h ⁻¹)	R ²
BF112-1-150	0.0126	0.9189
BF112-1-150-0.005	0.0266	0.9307
BF112-1-150-0.01	0.0209	0.9828
BF112-1-150-0.05	0.0338	0.9791
BF112-1-150-0.1	0.028	0.9648
BF112-4-150	0.2305	0.9758
BF112-4-150-0.005	0.1848	0.9921
BF112-4-150-0.01	0.2427	0.988
BF112-4-150-0.05	0.1818	0.997
BF112-4-150-0.1	0.2217	0.9503
BF112-7-150	0.0824	0.9523
BF112-7-150-0.005	0.0967	0.9862
BF112-7-150-0.01	0.2365	0.9878
BF112-7-150-0.05	0.2539	0.9889
BF112-7-150-0.1	0.2158	0.9823
BF112-10-150	0.1323	0.9549
BF112-10-150-0.005	0.0424	0.972
BF112-10-150-0.01	0.0413	0.9804
BF112-10-150-0.05	0.117	0.9628
BF112-10-150-0.1	0.0155	0.9658
BF112-13-150	0.0005	0.0091
BF112-13-150-0.005	0.0533	0.9511
BF112-13-150-0.01	0.0477	0.9468
BF112-13-150-0.05	0.0869	0.9877
BF112-13-150-0.1	0.067	0.8624

attributable synergistic effects that can include a layered structure, a low-energy band structure, and high BET surface area as well as the formation of composites (or heterojunction). Failure to use photocatalysts prevented CV degradation under irradiation provided by visible light; the BiO_mF_n/BiO_xI_y/GO composites' superior photocatalytic ability, compared with the other composites, is attributable to the fact that they utilize visible light in an efficient manner and achieves high electron–hole separation efficiency.

In general, the photodegradation of organisms through a semiconductor involves three reaction mechanisms, namely photocatalysis, photolysis, and dye photosensitization [28]. Photocatalytic decomposition in UV–Vis and semiconductor systems engenders different primary active species, some of which include hydroxyl, superoxide, and hydrogen radicals (H), as well as singlet oxygen and holes. Water dissociates on the surface of TiO₂ and in the subsequent molecular layers. Accordingly, Dimitrijevic et al. [29] suggested that water can function as (i) a charge stabilizer, through electron–hole recombination prevention; (ii) an electron acceptor, through H atom formation by reacting photogenerated electrons with surface protons, –OH₂⁺; and (iii) an electron donor, inducing water to react with photogenerated holes in order to yield OH radicals.

Combining GO with other materials results in the flow of electrons from a material to another (i.e., from a high Fermi level to a lower one); this thus results in Fermi energy level alignment at the GO–material interface [30]. Bai et al. [31] stated that the trapping measurement of active species that include superoxide (O₂^{•-}) and hydroxyl (OH) radicals is vital in catalyzing methylene blue degradation using ZnWO₄/graphene hybrids. As revealed by Wang et al. [32], O₂^{•-} and OH are the primary reactive species for degrading rhodamine B with BiVO₄/rGO. HO might be formed only through the e⁻ → O₂^{•-} → H₂O₂ → OH route. However, OH radicals were reportedly formed through the multistep O₂^{•-} reduction [33]. Research [31] reported that O₂^{•-}, instead of [•]OH, e⁻, or h⁺, mainly controlled the photocatalytic process. Lee et al. [5] revealed oxidation dominated the process of degrading CV using BiO_mX_n/BiO_pY_q (X, Y = Cl, Br, and I) under irradiation provided

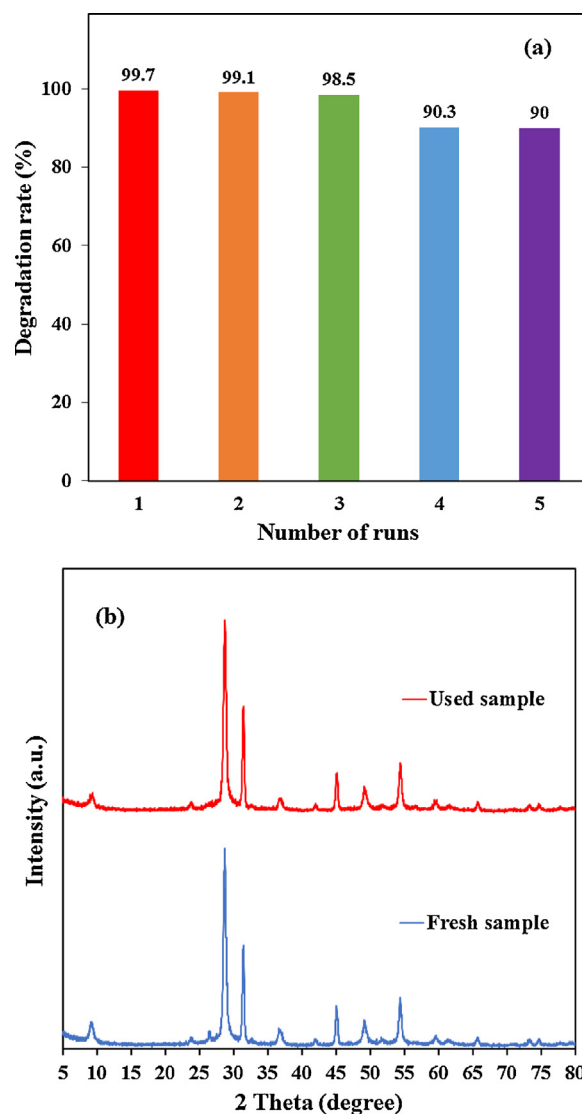


Fig. 8. (a) Cycling runs and (b) XRD patterns acquired before and after the photocatalytic degradation of CV in the presence of Bi₅₀O₅₉F₃₂/BiOI/GO.

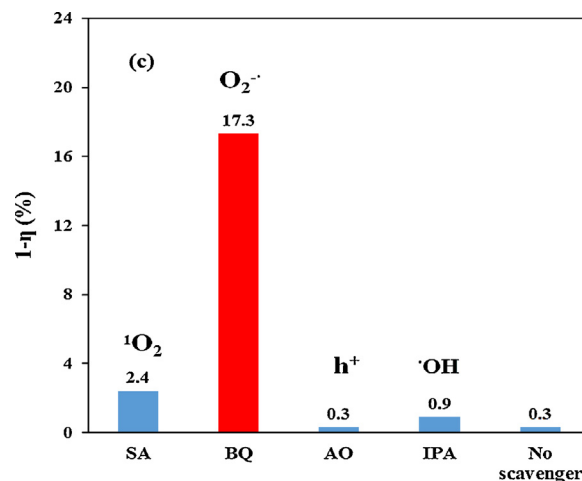


Fig. 9. CV concentration during photodegradation as a function of irradiation time observed for Bi₅₀O₅₉F₃₂/BiOI/GO under the addition of various scavengers: SA, IPA, AQ, and BQ.

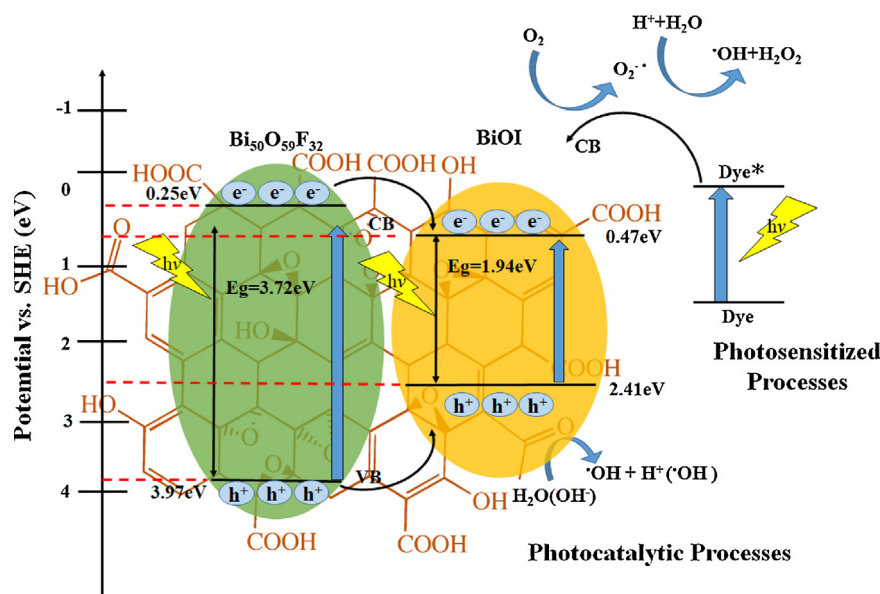
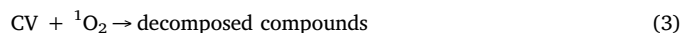


Fig. 10. Schematic of the band-gap structures of $\text{Bi}_{50}\text{O}_{59}\text{F}_{32}/\text{BiOI}/\text{GO}$.

by visible light; they identified the major active species to be $\text{O}_2^{\cdot-}$ and the minor active species to be OH and h^+ . The presented findings of the aforementioned studies signify that compared with the probability of $\text{O}_2^{\cdot-}$ formation, that of OH formation is considerably lower, but OH is highly robust and nonselective and induces several organic chemicals to be partially or completely mineralized.

This study reevaluated the action of active species in the photocatalytic reaction process by introducing several quenchers; thus, the relevant active species were thus scavenged. AO introduction did not influence the CV photocatalytic degradation (Fig. 9); however, the quenching of BQ, IPA, and SA evidently decreased the efficiency of the degradation. In CV photocatalytic degradation, $\text{O}_2^{\cdot-}$ is a major active species, whereas OH and $^1\text{O}_2$ are minor ones. Accordingly, the observed scavenger- and EPR-induced quenching effects indicate that $\text{O}_2^{\cdot-}$ plays a major part in the aforementioned degradation, whereas OH and $^1\text{O}_2$ play minor roles.

Fig. 10 details a decomposition pathway that is based on the preceding experimental results. Immediately after an electron arrives at the BiO_xX_y ($X = \text{Cl}, \text{I}$) conduction band, it engenders active oxygen species formation, resulting in CV dye decomposition. Both photosensitized and photocatalytic processes proceed concurrently (Fig. 10). Nevertheless, under conditions associated with photosensitized and photocatalytic reactions, electrons that are photogenerated and photosensitized react with photocatalyst-surface-dwelling oxygen to yield $\text{O}_2^{\cdot-}$ radicals; additionally, $\text{O}_2^{\cdot-}$ radicals react with H^+ ions and h^+ holes react with OH^- ions (or H_2O) to yield hydroxyl radicals. These subsequently result in hydroxyl radical production [34]. Exposing the system to irradiation conducted under visible light results in the continuous occurrence of this cycle [3]. To understand this unexpected result, the mechanism of $^1\text{O}_2$ formation was examined closely during the photoexcitation of $\text{BiO}_m\text{F}_n/\text{BiO}_x\text{I}_y/\text{GO}$ photocatalyst. $^1\text{O}_2$ can also be produced by transferring electrons between superoxide $\text{O}_2^{\cdot-}$ and cation species under suitable oxidizing power [35]. In semiconductor nanoparticles, photogenerated h^+ can function as a cation species oxidizing $\text{O}_2^{\cdot-}$. This $^1\text{O}_2$ production mechanism during ZnO photoexcitation was reported in a previous study [36]; Eqs. (1)–(3) present the CV decomposition process yielded by the derived oxidant species after several photo-oxidation cycles.



This study identified hydroxylated compounds for CV photocatalytic degradation in semiconductor systems under visible light [5]. Under irradiation by UV light, nitrogen-centered radical production was identified to precede *N*-dealkylation, and carbon-centered radical establishment was identified to precede dye chromophore structure demolition in the process of CV dye photocatalytic degradation [2,3,34]. The results of all the identified intermediates in the two topics were indicated to be the same under irradiation provided by UV or visible light. The photocatalytic and photosensitized processes are reported herein to proceed concurrently; nevertheless, $\text{O}_2^{\cdot-}$ results from the reaction, proceeding on the photocatalyst surface, of O_2 with photogenerated and photosensitized e^- , whereas OH results from $\text{O}_2^{\cdot-} - \text{H}^+$ and $\text{h}^+ - \text{OH}^-$ (or H_2O) reactions. Notably, the hydroxyl radical (HO^\cdot) is likely engendered only through the $\text{e}^- \rightarrow \text{O}_2^{\cdot-} \rightarrow \text{H}_2\text{O}_2 \rightarrow \text{OH}$ route, whereas the OH radical is engendered through a multistep $\text{O}_2^{\cdot-}$ reduction. Clearly, the major oxidants are OH rather than $\text{O}_2^{\cdot-}$ radicals. The reaction pathways of the proposed $\text{BiO}_m\text{F}_n/\text{BiO}_x\text{I}_y/\text{GO}$ -supported photocatalytic processes can guide dye decomposition operations.

4. Conclusions

This is the first study applying a simple hydrothermal method to execute $\text{Bi}_{50}\text{O}_{59}\text{F}_{32}/\text{BiOI}/\text{GO}$ -supported CV dye photocatalytic degradation under irradiation provided by visible light. The study noted excellent photocatalytic activity for the established $\text{Bi}_{50}\text{O}_{59}\text{F}_{32}/\text{BiOI}/\text{GO}$ composite during the degradation process. The composites could be sorted as follows in terms of rate constants: $\text{Bi}_{50}\text{O}_{59}\text{F}_{32}/\text{BiOI}/\text{GO} > \text{BiOF}/\text{BiOI}/\text{GO} > \text{BiOI} > \text{Bi}_{50}\text{O}_{59}\text{F}_{32}/\text{BiOI}/\text{BiO}_7\text{I}/\text{GO} > \text{BiOF} > \text{GO}$. The maximum rate constant associated with the $\text{Bi}_{50}\text{O}_{59}\text{F}_{32}/\text{BiOI}/\text{GO}$ photocatalytic activity was 0.2539 h^{-1} , which exceeded those of $\text{Bi}_{50}\text{O}_{59}\text{F}_{32}/\text{BiOI}$, BiOI , and $\text{Bi}_{50}\text{O}_{59}\text{F}_{32}$ by 1.1, 1.3, and 110 times, respectively. Thus, the derived $\text{Bi}_{50}\text{O}_{59}\text{F}_{32}/\text{BiOI}/\text{GO}$ is crucial for photocatalytic activity enhancement. For various scavengers, the noted quenching effects demonstrate that reactive $\text{O}_2^{\cdot-}$ has a notable role in the degradation of the applied CV. Overall, the catalytic activity and stability observed for the proposed composites were determined to be adequate; consequently, the composites can be authentic heterogeneous photocatalysts galvanized by visible light for the achievement of efficient organic pollutant degradation.

Acknowledgment

This research was supported by the Ministry of Science and Technology of the Republic of China (MOST-106-2113-M-142-001).

Appendix A. Supplementary data

Supplementary material related to this article can be found, in the online version, at doi:<https://doi.org/10.1016/j.mcat.2018.06.014>.

References

- [1] A. Kubacka, M. Fernández-García, G. Colón, Advanced nanoarchitectures for solar photocatalytic applications, *Chem. Rev.* 112 (2012) 1555–1614.
- [2] Y.R. Jiang, H.P. Lin, W.H. Chung, Y.M. Dai, W.Y. Lin, C.C. Chen, Controlled hydrothermal synthesis of $\text{BiO}_x\text{Cl}_y/\text{BiO}_m\text{I}_n$ composites exhibiting visible-light photocatalytic degradation of crystal violet, *J. Hazard. Mater.* 283 (2015) 787–805.
- [3] Y.R. Jiang, S.Y. Chou, J. Lin Chang, S.T. Huang, H.P. Lin, C.C. Chen, Hydrothermal synthesis of bismuth oxybromide-bismuth oxyiodide composites with highly visible light photocatalytic performance for the degradation of CV and phenol, *RSC Adv.* 5 (2015) 30851–30860.
- [4] W.L.W. Lee, W.H. Chung, W.S. Huang, W.C. Lin, W.Y. Lin, Y.R. Jiang, C.C. Chen, Photocatalytic activity and mechanism of nano-cubic barium titanate prepared by a hydrothermal method, *J. Taiwan Inst. Chem. Eng.* 44 (2013) 660–669.
- [5] W.W. Lee, C.S. Lu, C.W. Chuang, Y.J. Chen, J.Y. Fu, C.W. Siao, C.C. Chen, Synthesis of bismuth oxyiodides and their composites: characterization, photocatalytic activity, and degradation mechanisms, *RSC Adv.* 5 (2015) 23450–23463.
- [6] W.L.W. Lee, J.S. Lin, J.L. Chang, J.Y. Chen, M.C. Cheng, C.C. Chen, Photodegradation of CV over nanocrystalline bismuth tungstate prepared by hydrothermal synthesis, *J. Mol. Catal. A: Chem.* (2012) 361–362.
- [7] K. Yu, S. Yang, C. Liu, H. Chen, H. Li, C. Sun, S.A. Boyd, Degradation of organic dyes via bismuth silver oxide initiated direct oxidation coupled with sodium bismuthate based visible light photocatalysis, *Environ. Sci. Technol.* 46 (2012) 7318–7326.
- [8] S.Y. Chou, W.H. Chung, L.W. Chen, Y.M. Dai, W.Y. Lin, J.H. Lin, C.C. Chen, A series of $\text{BiO}_x\text{I}_y/\text{GO}$ photocatalysts: synthesis, characterization, activity, and mechanism, *RSC Adv.* 6 (2016) 82743–82758.
- [9] C.T. Yang, W.W. Lee, H.P. Lin, Y.M. Dai, H.T. Chi, C.C. Chen, A novel heterojunction $\text{Bi}_2\text{SiO}_5/\text{g-C}_3\text{N}_4$: synthesis, characterization, photocatalytic activity, and mechanism, *RSC Adv.* 6 (2016) 40664–40675.
- [10] H.P. Lin, C.C. Chen, W.W. Lee, Y.Y. Lai, J.Y. Chen, Y.Q. Chen, J.Y. Fu, Synthesis of $\text{SrFeO}_{3-x}/\text{g-C}_3\text{N}_4$ heterojunction with improved visible-light photocatalytic activities in chloramphenicol and crystal violet degradation, *RSC Adv.* 6 (2016) 2323–2336.
- [11] Jie Li, Ying Yu, Lizhi Zhang, Bismuth oxyhalide nanomaterials: layered structures meet photocatalysis, *Nanoscale* 6 (2014) 8473–8488.
- [12] X. Xiao, C. Xing, G. He, X. Zuo, J. Nan, L. Wang, Solvothermal synthesis of novel hierarchical $\text{Bi}_4\text{O}_5\text{I}_2$ nanoflakes with highly visible light photocatalytic performance for the degradation of 4-tert-butylphenol, *Appl. Catal. B: Environ.* (2014) 148–149.
- [13] W.L. Huang, Q.S. Zhu, DFT calculations on the electronic structures of BiOX ($X = \text{F}, \text{Cl}, \text{Br}, \text{I}$) photocatalysts with and without semicore Bi 5d states, *J. Comput. Chem.* 30 (2009) 183–190.
- [14] X. Xiao, C. Liu, R. Hu, X. Zuo, J. Nan, L. Li, L. Wang, Oxygen-rich bismuth oxyhalides: generalized one-pot synthesis, band structures and visible-light photocatalytic properties, *J. Mater. Chem.* 22 (2012) 22840–22843.
- [15] E. Keller, V. Kramer, A strong deviation from Vegard's rule: X-ray powder investigations of the three quasi-binary phase systems BiOX-BiOY ($X, Y = \text{Cl}, \text{Br}, \text{I}$), *Z. Naturforsch.* 60b (2005) 1255–1263.
- [16] Q. Xiang, J. Yu, M. Jaroniec, Graphene-based semiconductor photocatalysts, *Chem. Soc. Rev.* 41 (2012) 782–796.
- [17] H. Liu, W.R. Cao, Y. Su, Z. Chen, Y. Wang, Bismuth Oxyiodide-Graphene nanocomposites with High visible light photocatalytic activity, *J. Colloid Interface Sci.* 398 (2013) 161–167.
- [18] X.X. Wei, C.M. Chen, S.Q. Guo, F. Guo, X.M. Li, X.X. Wang, H.T. Cui, L.F. Zhao, W. Li, Advanced visible-light-driven photocatalyst BiOBr-TiO_2 -graphene composite with graphene as a nano-filler, *J. Mater. Chem. A* 2 (2014) 4667–4675.
- [19] I.V. Lightcap, T.H. Kosel, P.V. Kamat, Anchoring semiconductor and metal nanoparticles on a Two-dimensional catalyst mat. Storing and shuttling electrons with reduced graphene oxide, *Nano Lett.* 10 (2010) 577–583.
- [20] S. Song, B. Cheng, N. Wu, A. Meng, S. Cao, J. Yu, Structure effect of graphene on the photocatalytic performance of plasmonic $\text{Ag/Ag}_2\text{CO}_3$ -rGO for photocatalytic elimination of pollutants, *Appl. Catal. B: Environ.* 181 (2016) 71–78.
- [21] A. Bhirud, S. Sathaye, R. Waichal, C.J. Park, B. Kale, In situ preparation of N-ZnO/ graphene nanocomposites: excellent candidate as a photocatalyst for enhanced solar hydrogen generation and high performance supercapacitor electrode, *J. Mater. Chem. A* 3 (2015) 17050–17063.
- [22] W.S. Hummers, R.E. Offeman, Preparation of graphitic oxides, *J. Am. Chem. Soc.* 80 (1958) 1339.
- [23] X. Xiao, W.D. Zhang, Hierarchical $\text{Bi}_7\text{O}_9\text{I}_3$ micro/nano-architecture: facile synthesis, growth mechanism, and high visible light photocatalytic performance, *RSC Adv.* 1 (2011) 1099–1105.
- [24] H. Liu, Y. Su, Z. Chen, Z. Jin, Y. Wang, $\text{Bi}_7\text{O}_9\text{I}_3/\text{reduced graphene oxide}$ composite as an efficient visible-light-driven photocatalyst for degradation of organic contaminants, *J. Mol. Catal. A: Chem.* 391 (2014) 175–182.
- [25] F. Dong, Y. Sun, M. Fu, Z. Wu, S.C. Lee, Room temperature synthesis and highly enhanced visible light photocatalytic activity of porous BiOI/BiOCl composites nanoplates microflowers, *J. Hazard. Mater.* (2012) 219–220.
- [26] D. Chen, H. Feng, J. Li, Graphene oxide: preparation, functionalization, and electrochemical applications, *Chem. Rev.* 112 (2012) 6027–6053.
- [27] A. Chatzidakis, C. Berberidou, I. Paspaltsis, G. Kyriakou, T. Sklaviadis, I. Poullos, Photocatalytic degradation and drug activity reduction of chloramphenicol, *Water Res.* 42 (2008) 386–394.
- [28] C. Nasr, K. Vinodgopal, L. Fisher, S. Hotchandani, A.K. Chattopadhyay, P.V. Kamat, Environmental photochemistry on semiconductor surfaces. Visible light induced degradation of a textile diazo dye, naphthol Blue Black, on TiO_2 nanoparticles, *J. Phys. Chem.* 100 (1996) 8436–8442.
- [29] N.M. Dimitrijevic, B.K. Vijayan, O.G. Poluektov, T. Rajh, K.A. Gray, H. He, P. Zapol, Role of water and carbonates in photocatalytic transformation of CO_2 to CH_4 on titania, *J. Am. Chem. Soc.* 133 (2011) 3964–3971.
- [30] H.Y. Mao, S. Laurent, W. Chen, O. Akhavan, M. Imani, A.A. Ashkarran, M. Mahmoudi, Graphene: promises, facts, opportunities, and challenges in nanomedicine, *Chem. Rev.* 113 (2013) 3407–3424.
- [31] X. Bai, L. Wang, Y. Zhu, Visible photocatalytic activity enhancement of ZnWO_4 by graphene hybridization, *ACS Catal.* 2 (2012) 2769–2778.
- [32] Y. Wang, W. Wang, H. Mao, Y. Lu, J. Lu, J. Huang, Z. Ye, B. Lu, Electrostatic self-assembly of BiVO_4 -reduced graphene oxide nanocomposites for highly efficient visible light photocatalytic activities, *ACS Appl. Mater. Interfaces* 6 (2014) 12698–12706.
- [33] S.T. Huang, Y.R. Jiang, S.Y. Chou, Y.M. Dai, C.C. Chen, Synthesis, characterization, photocatalytic activity of visible-light-responsive photocatalysts $\text{BiO}_x\text{Cl}_y/\text{BiO}_m\text{Br}_n$ by controlled hydrothermal method, *J. Mol. Catal. A: Chem.* 391 (2014) 105–120.
- [34] H.J. Fan, C.S. Lu, W.L.W. Lee, M.R. Chiou, C.C. Chen, Mechanistic pathways differences between P25-TiO_2 and Pt-TiO_2 mediated CV photodegradation, *J. Hazard. Mater.* 185 (2011) 227–235.
- [35] W. He, H. Jia, W.G. Wamer, Z. Zheng, P. Li, J.H. Callahan, J.J. Yin, Predicting and identifying reactive oxygen species and electrons for photocatalytic metal sulfide micro-nano structures, *J. Catal.* 320 (2014) 97–105.
- [36] W. He, H.K. Kim, W.G. Wamer, D. Melka, J.H. Callahan, J.J. Yin, Photogenerated charge carriers and reactive oxygen species in ZnO/Au hybrid nanostructures with enhanced photocatalytic and antibacterial activity, *J. Am. Chem. Soc.* 136 (2014) 750–757.